Earth and Planetary Science
https://journals.nasspublishing.com/index.php/eps

RESEARCH ARTICLE

Magma Degassing and Gold Mineralization in the Alkaline Intrusion-Hosted Gilt Edge Gold Deposit, Northern Black Hills, South Dakota, USA

John A. Groff[1,2*]

1. South Dakota School of Mines and Technology, 501 East St. Joseph Street, Rapid City, SD 57701, USA
2. Tuscaloosa Academy, 420 Rice Valley Road, Tuscaloosa, AL 35046, USA

Abstract: Gold mineralization in the Gilt Edge deposit was closely associated with magmatic differentiation and the formation of a Tertiary alkaline intrusive complex within the Lead–Deadwood dome. Fluid inclusions and trace element geochemistry were used to study fluid evolution and determine sources. Quartz disseminated in unaltered trachyte porphyry hosts two populations of primary inclusions: 1) hypersaline i S–L–V ± a red hematite crystal and 2) mixtures of L–V and V– L that record phase separation at ~700ºC. Whereas samples of hydrothermal quartz collected from ore zones within and beyond structures (e.g., fault and breccia zones) contain dominant populations of V–L and L–V inclusions, respectively. Mineralization in structures formed from complex fluids of magmatic origin based on inclusions containing five transparent salt crystals and opaque crystals with cubic and round habits that have homogenization temperatures (T_h) ≤ 650ºC and salinities ≤ 63 wt.% NaCl equiv. In contrast, broader areas of disseminated mineralization in argillized and propylitized rocks contain hydrothermal quartz hosting large populations of L–V inclusions with T_h of 200º–360ºC and salinities of 10–30 wt.% NaCl equiv., which reflect fluid mixing. Trace element concentrations are significantly higher in samples from structures and define zones of near surface Ag–As–Zn–Pb and deep Au–W–Mo–Cu. Whereas low trace element concentrations characterize propylitized quartz trachyte porphyry, except for high concentrations of Sb and Hg that occur at depth and likely track the retreat of isotherms as the hydrothermal system collapsed. These data show that during differentiation in a deep magma chamber, volatile-rich low-density fluids were periodically degassed into preexisting structures that were reactivated. Gold deposition during four stages of mineralization likely occurred due to boiling, changes in oxygen fugacity, and fluid mixing.

Keywords: Fluid inclusion microthermometry; Magma differentiation; Whole-rock geochemical data; Alkaline intrusive complex

*Corresponding Author:
John A. Groff,
South Dakota School of Mines and Technology, 501 East St. Joseph Street, Rapid City, SD 57701, USA;
Tuscaloosa Academy, 420 Rice Valley Road, Tuscaloosa, AL 35046, USA;
Email: jgroff@tuscaloosaacademy.org

Received: 10 June 2024; **Received in revised form:** 13 August 2024; **Accepted:** 20 August 2024; **Published:** 14 October 2024

Citation: Groff, J.A., 2024. Magma Degassing and Gold Mineralization in the Alkaline Intrusion-Hosted Gilt Edge Gold Deposit, Northern Black Hills, South Dakota, USA. *Earth and Planetary Science*. 3(2): 82–105. DOI: https://doi.org/10.36956/eps.v3i2.1125

DOI: https://doi.org/10.36956/eps.v3i2.1125

1. Introduction

Gold deposits associated with alkaline igneous rocks share characteristics that suggest a broadly similar process operated during ore genesis [1, 2]. Mineralization is controlled by structure [3–5] and occurred late in the formation of igneous complexes [6, 7]. There are multiple stages of mineralization [8–10], Au–Ag tellurides are part of the ore assemblage [11, 12], and potassium metasomatism is extensive [5, 13, 14]. The combination of fluid inclusion and stable isotope data support a significant magmatic component to ore fluids [7, 15]. An important point is that primary iron-oxides in the mineral paragenesis and ground mass of igneous rocks suggest the magmas were oxidized [1, 16], which precluded early deposition of pyrite. Therefore, ore metals and volatile phases partitioned into a low-density fluid [17] that accumulated at the magma chamber's apex. An oxidized magma and degassing during the differentiation of alkaline rocks are integral parts of genetic models for associated ore deposits, since the low-density volatile-rich phase served to concentrate and transport metals [18, 19].

The Gilt Edge deposit in the northern Black Hills of South Dakota, USA (**Figure 1**) shares many of the characteristics listed above. Four stages of mineralization have been documented with gold occurring in the native form and Au–Ag tellurides [20]. Mineralization is controlled by structure, occurred late during the formation of an intrusive complex, and there is extensive potassium metasomatism in some breccia and fracture zones [21]. Primary iron-oxide minerals are part of the ore assemblage and also occur disseminated in the groundmass of igneous rocks, which suggests oxidized magmas were involved in formation of a significant orebody with past proven and probable reserves of 49 million tonnes 1.28 g/t Au [21, 22]. Mining operations ceased in 1998 and total gold production was 254,000 oz [21, 22].

What makes the Gilt Edge deposit particularly amenable to fluid inclusion study is that the evolved alkaline intrusions contain small amounts of quartz as a primary phase, in addition to hydrothermal quartz that is intergrown with sulfidic ore. Therefore, fluid inclusion petrography and microthermometric analyses were undertaken to determine the characteristics of inclusions hosted by both primary quartz disseminated in unaltered trachyte porphyry and different generations of hydrothermal quartz obtained from drill core and surface outcrops. The potential for magma degassing during mineralization was addressed by documenting the types of fluid inclusions hosted by hydrothermal quartz from a variety of geological settings (e.g., low-grade disseminated ore in argillized and propylitized rocks vs. high-grade ore associated with potassium metasomatized rocks in fracture zones and intrusion breccia). Fluid inclusions in late-stage fluorite were also analyzed to determine changes in hydrothermal fluids with time.

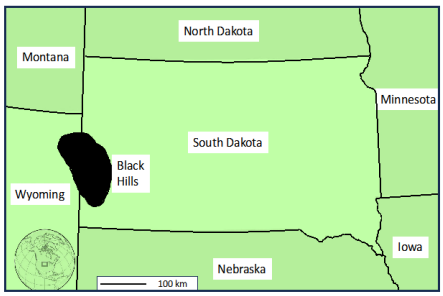

Figure 1. Map showing the location of the northern Black Hills relative to adjacent states and a general location within the United States (lower left inset).

As there is a lateral zoning of metals across the deposit, there could also be a vertical zoning to support a deep source. The lateral zoning is based on geochemical data generated through rock-chip sampling of outcrops that show high Hg concentrations ($\leq$ 36 ppm) on the periphery of the intrusive complex; a Cu–Mo anomaly at the west/southwest (W/SW) margin of the deposit; and a broad zone of As enrichment that extends beyond the deposit [23]. Therefore, whole-rock geochemical analyses of drill core are reported for a 150-m vertical section of the Dakota Maid fracture zone and then compared with a deposit scale 460-m vertical section for different rock and alteration types.

2. Geology

The Black Hills formed as a result of Laramide deformation that created a regional dome containing a core of Precambrian metamorphic rocks, which is crosscut by an east to west (E–W) trending belt of Tertiary intrusions [24]. Proterozoic metamorphic rocks in the Lead–Deadwood dome consist of garnetiferous quartz–mica

schist, amphibolite, banded chert, phyllite, and metamorphosed banded iron formation containing cummingtonite and grunerite[24, 25]. The Precambrian strata experienced two deformational events that occurred during prograde and retrograde metamorphism associated with the emplacement of the 1.84 Ga Harney Peak granite[25]. This deformation is recognized by multiple isoclinal and sheath fold events that were coeval with ductile and brittle shearing[26]. A prominent foliation (e.g., NW–W strike and 40o–55o SW dip) is formed by the alignment of micaceous minerals and near-vertical jointing[23]. An angular unconformity separates Precambrian rocks from the overlying Cambrian Deadwood Formation comprised of a basal quartzite and upper sequence of metamorphosed sandstone–shale–carbonates.

The E–W trending belt of Tertiary intrusions is part of a larger 60–46 Ma igneous province that extends across Wyoming, Montana, and into Alberta, Canada[27, 28]. Igneous activity was related to subduction of the Farallon and Kula plates beneath the North American plate, with a change from compressional to extensional tectonism 53 Ma[2, 27]. The oldest intrusive rocks around the Gilt Edge mine are represented by a 60.5 $\pm$ 3 Ma laccolith of hornblende trachyte porphyry (Thtp) and smaller sills[23]. Flow layering near the margins of the laccolith is evident by the alignment of hornblende and plagioclase phenocrysts[23]. Hand samples of Thtp have a distinct gray–green color and are finer-grained compared with the other Tertiary igneous rocks in the area (**Table 1**).

The emplacement of subsequent intrusions formed an igneous complex within the mine area consisting of multiple generations of trachyte porphyry (Ttp) and quartz trachyte porphyry (Tqtp), compared with post-mineralization rhyolite dikes[21, 23]. Chemical analyses of mineral separates document a change in the composition of feldspars from Or_{30} (Thtp) to Or_{68} (rhyolite)[23]. Two main bodies of Ttp are recognized as the Dakota Maid and Rattlesnake stocks (**Figure 2**). Xenoliths of Dakota Maid Ttp in the Rattlesnake Ttp establish an age relationship[29]. A textural difference between the two involves phenocryst sizes, with the Dakota Maid being coarser grained (**Table 1**). As Ttp is the dominant host of mineralization, it is highly altered and intensely fractured to brecciated.

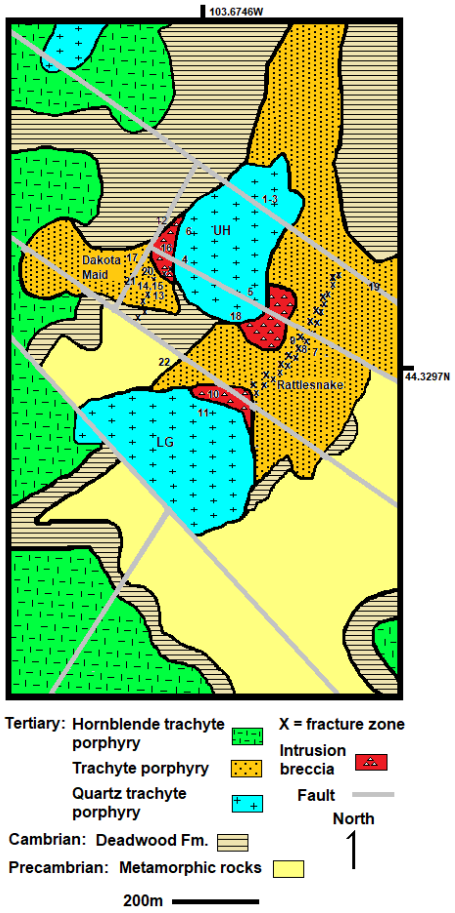

Figure 2. Geologic map of the Gilt Edge deposit after MacLeod and Barron[21]. Sample numbers are indicated by numerical values, UH = the Union Hill stock, LG = the Langley stock, and the Dakota Maid and Rattlesnake trachyte porphyries are labelled.

Two stocks of Tqtp (the Union Hill and Langley) within the mining area are partly ringed by breccia that formed during emplacement of the stocks (e.g., intrusion breccia in **Figure 2**), but there is no crosscutting relationship between the stocks. However, both have chilled margins and contain xenoliths of Ttp[21, 23]. Hand samples of Tqtp are easily identified due to having a distinct pink–gray cast and containing quartz eyes $\leq$ 5 mm disseminated in the groundmass (**Table 1**). As stocks of both Tqtp and Ttp have NE elongations that are subparallel to NE-trending fracture zones, their emplacement was likely controlled by preexisting structure in the Precambrian rocks[21]. Fracture zones contain significant amounts of ore and are recognized as linear features with varying degrees of fracture intensity that increases

Table 1. Descriptions of Tertiary igneous rocks that occur around and in the Gilt Edge deposit [23, 29].

Composition	Intrusion type	Phenocrysts	Size	Groundmass	Color	Comments
Hornblende trachyte	Laccolith, sills	Plagioclase, hornblende	0.5–5 mm	Cryptocrystalline K-feldspar	Gray–green	Peripheral to deposit
Trachyte	Stocks, sills, dikes	Perthite, minor plagioclase	10.5 mm–5 cm	Microcrystalline K-feldspar	Gray	Highly altered and fractured
Quartz trachyte	Stocks, dikes	Perthite, plagioclase, sanidine, quartz	0.5–5 cm	Cryptocrystalline K-feldspar	Pink–gray	Only altered and mineralized near structures
Rhyolite	Dikes	Sanidine, quartz	<0.5 mm	Aphanitic to microcrystalline	White	Unaltered, barren

to form tectonic breccia. Although fracture zones are laterally continuous and extend beyond the deposit, mineralized widths in the mine area are commonly a few meters. However, these widths more than double at structural intersections.

The youngest Tertiary intrusions are small dikes of rhyolite that intrude older igneous rocks. These fine-grained dikes are uncommon and readily identified in the field due to appearing as white porcelain (**Table 1**). The dikes postdate mineralization due to being unaltered, weakly jointed, and barren.

Alteration is most intense within NE- and NW-trending fracture zones, tectonic breccia that formed at structural intersections, and intrusion breccia partly ringing the Tqtp stocks [21, 23]. Areas of potassium metasomatism consist of intergrown fine-grained adularia and lesser hydrothermal quartz that almost completely replace Ttp in fracture zones. Whole-rock geochemical data record depletion of Na_2O and CaO with enriched K_2O contents ≤ 12 wt.% [21]. Argillic alteration increased the porosity of rocks [23] and is recognized by the presence of kaolinite in large sections of Ttp in a structurally complex area between the Tqtp stocks. Finally, propylitic alteration within the deposit is mostly restricted to the interior of Tqtp stocks and can be identified by epidote and calcite $\pm$ chlorite [21]. Although ore zones occur in all three types of alteration, the highest grades are associated with potassium metasomatism in fracture zones and breccia. This is represented by open-space fillings in fracture zones and the matrix to breccia, compared with disseminated ores in broader areas of propylitic and argillic alteration.

3. Mineralization

Two periods of mineralization are indicated by geologic relationships [21]. The first period is devoid of gold, predates emplacement of the Tqtp stocks, and is recognized by closely spaced quartz veins ($\leq$ 2-cm wide) containing 1–2% pyrite with lesser amounts of chalcopyrite and molybdenite in Ttp (**Figure 3**). At the margins of Tqtp stocks, quartz veins in Ttp are truncated and occur as clasts within the adjacent intrusion breccia and/or xenoliths in Tqtp.

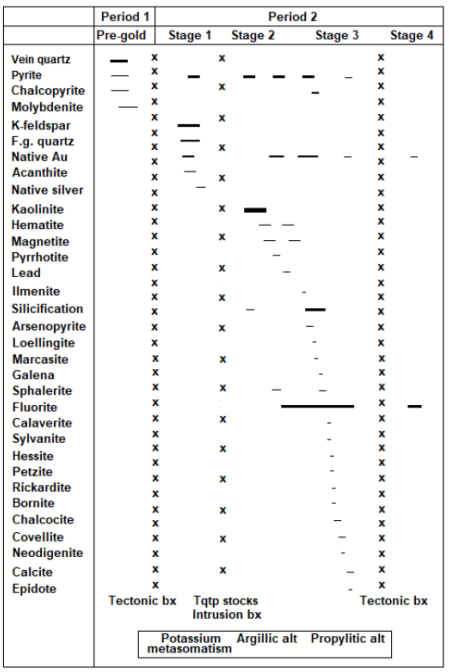

Figure 3. Paragenesis of mineralization for the Gilt Edge deposit. Modified from Groff and Paterson [20] using data from Mukherjee [23] and the current study. Discrete episodes of deposition for minerals such as pyrite are indicated by separate lines. Abbreviations: F.g. quartz = fine-grained quartz intergrown with adularia; bx = breccia; and alt = alteration.

The second period of economically important mineralization is associated with the emplacement and evolution of the Tqtp stocks[21]. Ores are sulfide-rich consisting of pyrite veins, the matrix to breccia, and roof pendants of highly argillized Cambrian Deadwood hornfels containing $\leq$ 20% disseminated pyrite. Gold mineralization occurred in four stages with distinct assemblages of sulfide, iron-oxide, or telluride minerals (**Figure 3**). Stage 1 consists of pyrite–native gold–acanthite mineralization (**Figure 4a**). Stage 2 occurs in samples from fracture zones, breccia, and the Tqtp stocks. It is represented by an assemblage of pyrite–magnetite–hematite–chalcopyrite–arsenopyrite (**Figure 4b**). Native gold occurs as inclusions in arsenopyrite[23] and heals fractured pyrite crystals. Greater concentrations of magnetite occur as veins and disseminations at depths $\geq$ 300 m that are localized in the Rattlesnake fracture zone near contacts of the Tqtp stocks[21]. Stage 3 is characterized by base metal sulfides (**Figure 4c,d**), Au–Ag tellurides, and fluorite. The tellurides surround pyrite crystals or fill vugs (**Figure 4e**) and rarely rim early particles of native gold **(Figure 4f**). This mineralization occurs in samples from breccia, fracture zones, and areas of the Tqtp stocks near a geologic contact or intrusion breccia. Fluorite occurs as veins, open-space fillings in argillized rocks, and rarely as the matrix to breccia. Finally, Stage 4 mineralization is limited to breccia samples and consists of native gold veinlets 2–3 μm wide that crosscut tellurides (**Figure 4g**). Although uncommon, fluorite veinlets do crosscut the clasts and matrix in breccia zones.

4. Materials and methods

4.1 Fluid inclusions

Quartz and purple fluorite obtained from both drill core and pit samples were used for fluid inclusion microthermometric analyses (**Appendix A**). All samples were categorized according to rock type, alteration, and structural setting (e.g., fracture zone, tectonic breccia, breccia that formed during emplacement of Tqtp stocks, or outside of structural zones). Type samples were also selected to represent zones of potassium metasomatism and argillic and propylitic alteration. Then doubly polished sections for fluid inclusion analyses were prepared using a slow-speed oil-cooled carbide saw and cleaned after each polishing stage in an ultrasonic bath.

Fluid inclusions were studied using a Zeiss microscope (40x objective and 12x oculars) and USGS gas-flow stage. The inclusions were classified as primary or secondary based on criteria established by Roedder[30]. Inclusions ranged from 4–50 μm and averaged 15 μm. Within each sample, assemblages were identified that represented petrographically associated groups of coeval inclusions[31–33]. It is inferred that fluid inclusions comprising a single assemblage formed at essentially the same time and under similar conditions.

Although heat resistant silica glass windows were used in the stage during analyses of primary quartz in unaltered Ttp, optics progressively degraded and homogenization temperatures (T_h) could not be determined accurately above 700°C. Routine calibration of the stage was completed using synthetic standards having different melting points, in addition to distilled water and laboratory-created chips containing fluid inclusions of pure water and CO_2. The presence, or absence, of CO_2 in inclusions was based on the results of petrographic study and freezing/heating analyses. Cursory nonquantitative analyses of select fluid inclusions by Dr Bob Burruss (USGS Denver) using a Raman microprobe were completed to determine if CO_2 was the only gas phase.

4.2 Geochemical data

The metal content of different rock and alteration types was determined using whole-rock geochemical data compiled by Brohm Mining corporation. Mine geologists split and sampled drill core at intervals of 0.5–15 m based on contacts between different rock types, alteration, and the width of mineralized zones. The core was then sent to a commercial lab and prepared for whole-rock geochemical analyses that used atomic absorption and ICP–AES methods. Fire assay was used to determine the concentration of gold. Rock samples were crushed, pulverized, and sieved to obtain a powder with particle sizes $\leq$ 80 μm. This powder was digested using aqua regia prior to analysis. Blanks and certified reference materials were run after a specific number of metal analyses. The analyzed metals included Au, Ag, Cu, W, Sn, Pb, Zn, Sb, Hg, As, and F. A total of 4089 m of drill core that

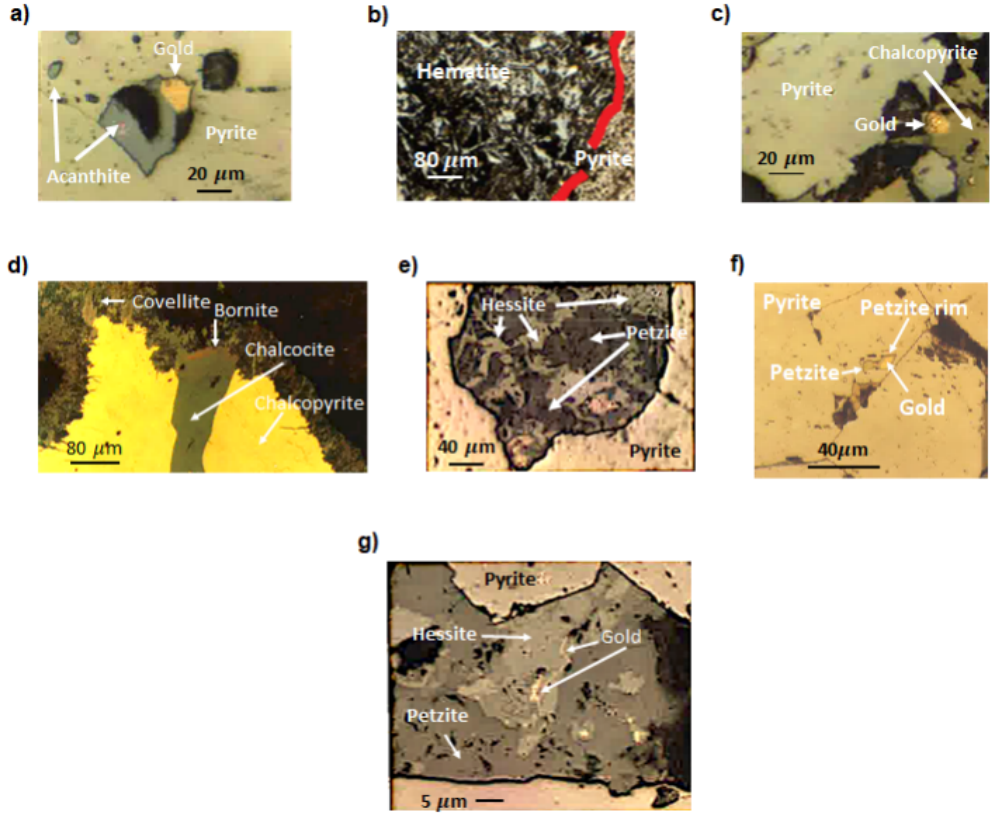

Figure 4. Photomicrographs showing ore textures for different stages of mineralization in period 2: **a**) Stage 1 acanthite, native gold, and pyrite. **b**) Stage 2 pyrite replacing primary hematite in the Union Hill stock. The boundary between minerals is highlighted by a red line. **c**) Stage 3 native gold in chalcopyrite adjacent to pyrite. **d**) Stage 3, chalcopyrite crosscut by chalcocite and rimmed by covellite. Bornite occurs near where the chalcocite vein meets the covellite rim. **e**) Stage 3 gold and silver tellurides that fill a vug in pyrite. **f**) Stage 3 petzite rimming native gold in pyrite. **g**) Stage 4 gold veinlet 1 to 2-m-wide that crosscuts hessite and petzite.

spans a vertical interval of 460 m through the deposit was sampled and analyzed.

5. Results

5.1 Fluid inclusions

Primary quartz in unaltered Ttp

Doubly polished sections were prepared for unaltered Ttp 10-m east of the Rattlesnake fracture zone (sample 7). Petrographic study identified a small population of quartz grains 2 mm across with embayed edges that occur as disseminations in a groundmass dominated by K-feldspar. Individual quartz grains host primary fluid inclusions that are either hypersaline (S–L–V) or two-phase with highly variable phase ratios; the S–L–V inclusions are not intermixed with the two-phase inclusions. The S–L–V inclusions have ovoid to rectangular shapes and are randomly distributed in quartz. A small number of these inclusions contained liquid CO_2 as a narrow rim around the vapor bubble. Salt crystals with cubic and round shapes were most likely halite and sylvite (**Figure 5a**), respectively, as the round crystals always melted at lower temperatures. Salinities for 10 of these inclusions are 32–78 wt.% NaCl equiv. and two inclusions homogenized to the liquid phase [$T_{h(L)}$] prior to halite melting at $\geq$ 600oC (**Figure 6a,b**). However, most still had a small vapor bubble at 700oC. Salinities of < 10 wt.% NaCl equiv. were recorded for the two-phase vapor-poor inclusions, as no ice melting could be observed in vapor-rich inclusions. Some polyphase inclusions contained a transparent red hematite crystal (trigonal to tabular shape) or translucent reddish-brown crystal (tabular to ovoid shape with irregular edges).

Cursory Raman microprobe analyses also detected CO_2 and N_2 in vapor bubbles of some polyphase inclusions.

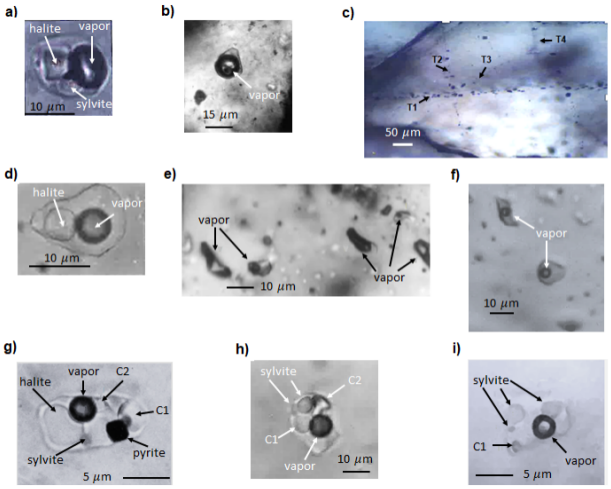

Figure 5. Photomicrographs of different types of primary and secondary fluid inclusions. **a**) Primary quartz in unaltered Ttp containing a primary halite and sylvite-bearing inclusion. **b**) Primary vapor-rich inclusion hosted by primary quartz in unaltered Ttp. **c**) Multiple trains (T1, T2, T3, T4) of crosscutting vapor-rich or all-vapor inclusions in a quartz-veined trachyte xenolith within Tqtp. **d**) Primary halite-bearing inclusion in hydrothermal quartz. **e**) Primary vapor-rich and liquid-rich inclusions in hydrothermal quartz. **f**) Primary liquid-rich inclusion hosted hydrothermal quartz in Tqtp. **g**) Complex primary inclusion in hydrothermal quartz containing an opaque cube (pyrite), halite, sylvite, and two unknown crystals (C1 and C2). **h**) Primary inclusion in hydrothermal quartz containing two sylvite crystals, an unknown crystal (C1), and an unknown birefringent crystal (C2). **i**) Primary inclusion in hydrothermal quartz that contains multiple sylvite crystals, which melted at the same temperature, and an unknown crystal (C1).

Other quartz grains host primary two-phase inclusions that have phase ratios ranging from 5–100% vapor (**Figure 5**b). The inclusions containing > 50% vapor (V–L) are dominant, and a very-small number of both L–V and V–L inclusions contain a cubic halite crystal. Freezing runs did not identify CO_2, but cursory Raman microprobe analyses did detect CO_2 and N_2 in some V–L inclusions. Although the V–L inclusions lack narrow reentrants necessary for determining accurate homogenization to the vapor phase [$T_{h(V)}$], it was clear that some inclusions had not homogenized at 700oC. Ice melting could not be observed in any vapor-rich inclusions.

Hydrothermal quartz

There are different primary textures for pre-ore and hydrothermal quartz. Pre-ore (Period 1) quartz veins in Ttp xenoliths are relatively coarse-grained ($\leq$ 6 mm) and individual crystals are transparent. In contrast, quartz intergrown with adularia in high-grade ore zones is translucent and fine-grained ($\leq$ 2 mm crystals). Disseminated and low-grade ore in argillized and propylitized Tqtp contains disseminated 3–5 mm irregular quartz blebs intergrown with alteration minerals. A final generation of pyrite-rich microcrystalline quartz occurs as the matrix to high-grade ore in tectonic breccia. It is easily recognized in the field due to having a tan to medium-brown color, chert-like appearance, and miarolitic cavities $\leq$ 5 mm (**Figure 7**a).

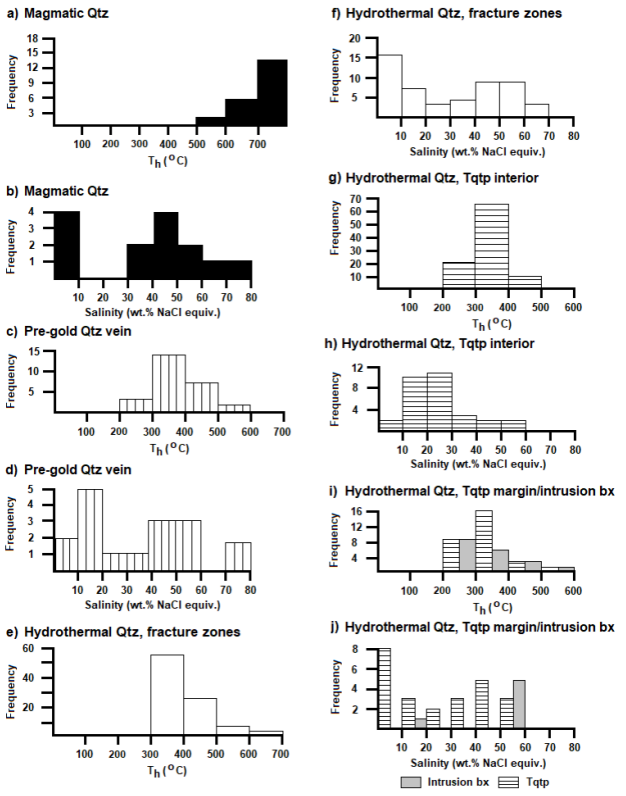

Figure 6. Histograms of Th and salinity for primary fluid inclusions in **a**,**b**) primary quartz (Qtz) in unaltered Ttp; **c**,**d**) a pre-gold quartz vein in a Ttp xenolith (sample 18) within Tqtp; **e**,**f**) hydrothermal quartz from fracture zones; **g**,**h**) hydrothermal quartz from the interior of the Union Hill Tqtp stock; and **i**,**j**) hydrothermal quartz from the intrusion breccia and an adjacent ore zone in the Langley Tqtp stock. Note that the Th > 700°C for primary quartz in unaltered Ttp could not be accurately determined because poor optics precluded measurement of homogenization to the liquid or vapor phase.

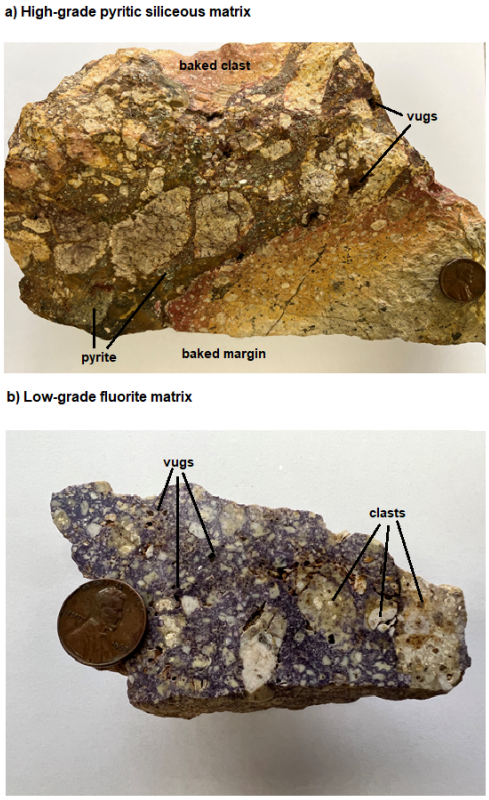

Figure 7. Photographs of **a**) tectonic breccia cemented by pyrite-rich microcrystalline quartz. Note that a reddish discoloration of the clasts is due to high-temperature baking and a 2.5-cm baked zone extends into the country rock. Miarolitic cavities are indicated by 'vugs.' **b**) In contrast, Ttp clasts are pristine in a breccia cemented by fluorite that does not contain visible pyrite. Note that the discolored areas in the breccia are due to secondary iron-oxide minerals, not alteration. The coin in both photographs has a diameter of 1.9 cm.

There are distinct differences between assemblages of secondary and primary fluid inclusions in pre-ore Period 1 quartz veins (sample 18). Individual quartz grains contain multiple trails of crosscutting inclusions that are either V–L (>70% vapor) or one-phase vapor (**Figure 5c**). However, no noticeable change to the inclusions occurred with freezing and heating. In contrast, primary fluid inclusion assemblages consist of a mixture of L–V, V–L, and S–L–V (**Figure 5d,e**) $\pm$ a small (3 μm) sub-round opaque crystal. Inclusions that are part of a single assemblage in one quartz crystal record ranges in T_h up to 60°C. However, the overall range for $T_{h(L)}$ of inclusions in four fluid inclusion assemblages hosted by four quartz crystals is 237°–582°C (**Figure 6c**). Salinities for the different types of inclusions range from 4–78 wt.% NaCl equiv. (**Figure 6d**).

Four samples from fracture zones contain ore stage hydrothermal quartz that is intergrown with sulfides, compared with sample 8 that contains fine-grained quartz intergrown with adularia. Fluid inclusion assemblages in all the samples consist of mixtures of S–L–V, L–V, and V–L. Individual fluid inclusion assemblages have ranges in T_h of 30°–60°C but when all the microthermometric data are plotted, the largest population of T_h is between 300°–500°C (**Figure 6e**). As the shapes of V–L inclusions were not ideal for determining $T_{h(v)}$ accurately, the best estimate for all samples is 385°–500°C. Salinities for different types of inclusions range from 8–63wt.% NaCl equiv. (**Figure 6f**), with eutectic types for L–V inclusions ranging from –23° to –32°C. No CO_2 was detected during petrographic study or microthermometric analyses.

Gold-mineralized samples from the interior of the Union Hill Tqtp stock contain assemblages of primary L–V fluid inclusions (**Figure 5f**) hosted by quartz blebs. Inclusions with halite $\pm$ sylvite crystals are rare and homogenization always occurred to the liquid phase. Individual assemblages of inclusions record ranges in T_h of 20°–30°C. Most inclusions have T_h of 250°–370°C and salinities are dominantly 10–30 wt.% NaCl equiv. (**Figure 6g,h**), with eutectic temperatures of –21° to –24°C.

An interesting result is that the same quartz blebs in the Union Hill (sample 6) and Langley (sample 11) Tqtp stocks adjacent to gold-bearing zones of intrusion breccia host multiple types of fluid inclusions. Individual assemblages contain mixtures of L–V, V–L, and S–L–V $\pm$ sylvite crystals. These inclusions homogenized to the liquid phase, vapor phase, and/or by halite dissolution. Salinities vary and T_h record ranges $\leq$ 70°C in some fluid inclusion assemblages (**Figure 6i,j**). Due to V–L inclusions having regular shapes, the best estimate for $T_{h(v)}$ is 280°–350°C. No CO_2 was detected during petrographic study or microthermometric analyses.

The same mixture of primary L–V, V–L, and S–L–V inclusions is hosted by hydrothermal quartz in the matrix of breccia that formed during intrusion of the Langley Tqtp stock (sample 10). Homogenization to the liquid phase occurred at 242°–580°C, with ranges of $\leq$ 70°C for some fluid inclusion assemblages, and mea-

sured salinities were 12–58 wt.% NaCl equiv. (**Figure 6i,j**). No CO_2 was detected during petrographic study or microthermometric analyses.

Fluorite

Sample 10 from the Langley Tqtp stock intrusion breccia also contains light-purple fluorite veinlets that crosscut the siliceous matrix and clasts. These veinlets are mineralized based on the identification of disseminated pyrite and chalcopyrite. Primary fluid inclusions hosted by the fluorite are dominantly L–V but 10% have a halite crystal and rare inclusions contain both a halite and sylvite crystal. Inclusions composing individual assemblages record ranges in T_h of 15°–30°C, with overall ranges for T_h and salinities of 290°–472°C and 14–45 wt.% NaCl equiv. (**Figure8**), respectively. No CO_2 was detected during petrographic study or microthermometric analyses.

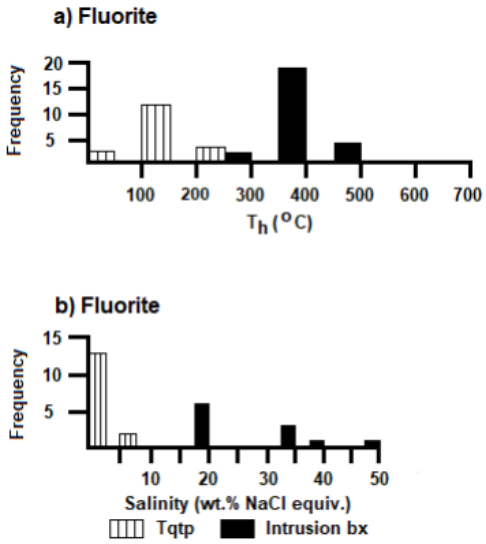

Figure 8. Histograms of Th and salinity for primary fluid inclusions hosted by fluorite veinlets cutting intrusion breccia compared with fluorite cubes in argillized Tqtp.

As a comparison, fluid inclusions hosted by fluorite disseminated in argillized Union Hill Tqtp (sample 4) were analyzed. This fluorite occurs as well-formed cubes that have a deep-purple color. Primary fluid inclusions are almost entirely L–V, with halite crystals being rare and no sylvite crystals were identified. Individual assemblages record ranges in T_h of 10°–20°C. There is no overlap with salinity data for the fluorite veinlets that crosscut intrusion breccia and T_h are lower overall for inclusions hosted by fluorite cubes in argillized Tqtp (**Figure 8**). One fluid inclusion assemblage in a fluorite cube contained inclusions with T_h of 85°C and salinity of 0 wt.% NaCl equiv. Eutectic temperatures of L–V inclusions display a limited range of –21° to –22°C.

5.2 Alteration types

Microthermometric data for three ore-samples were selected to represent the characteristics of fluids that produced propylitic (sample 2) and argillic (sample 4) alteration compared with potassium metasomatism (sample 8). The hydrothermal quartz in samples of propylitized and argillized Tqtp occurs as grains intergrown with secondary minerals or is oriented along clay partings. Primary fluid inclusion assemblages in the sample for propylitic alteration are all L–V and ranges in T_h for individual assemblages are $\leq$ 20°C. The overall ranges in T_h and salinity are 201°–321°C and 12–24 wt.% NaCl equiv. (**Figure 9a,b**), respectively.

The primary fluid inclusion assemblages studied in the argillic sample were dominantly L–V, with 10% having a halite crystal and only one sylvite-bearing inclusion. Homogenization was to the liquid phase at temperatures of 212°–460°C, excluding halite dissolution in one inclusion at 490°C (**Figure 9a,b**). Ranges in T_h for individual assemblages are $\leq$30°C, excluding the homogenization by halite dissolution. Whereas salinities ranged from 4–42 wt.% NaCl equiv., excluding the value of 54 wt.% NaCl equiv. for homogenization by halite dissolution.

The fluid inclusion assemblages hosted by quartz intergrown with adularia (potassium metasomatism) are characterized by S–L–V inclusions. These comprise nearly half of all inclusion assemblages. Sylvite crystals are common and V–L inclusions occur in equal or greater numbers compared with L–V inclusions. Overall, there are large ranges in T_h and salinity of 383°–630°C and 12–65 wt.% NaCl equiv. (**Figure 9c,d**). Homogenization occurred to the liquid phase, vapor phase, and by halite dissolution. However, $T_{h(V)}$were difficult to measure accurately due to fluid inclusions having regular shapes and the best estimate is 400°–500°C. There was a larger range in T_h for individual fluid inclusion assemblages of $\leq$ 60°C compared with the other alteration types.

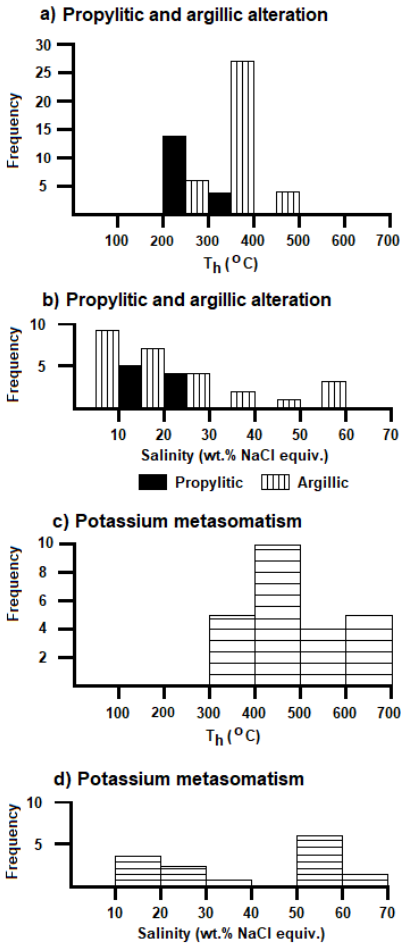

Figure 9. Histograms of Th and salinity for primary fluid inclusions in **a**,**b**) propylitized or argillized Tqtp and **c**,**d**) Ttp that has undergone potassium metasomatism.

5.3 Distribution of fluid inclusion types

Qualitative observations made during the petrographic study of hydrothermal quartz suggested that certain types of fluid inclusions were most common in specific geologic settings. Therefore, point counts of 120–350 primary fluid inclusions hosted by hydrothermal quartz were completed for eight ore samples. Quartz in three samples from the interior of the Union Hill Tqtp stock, beyond structural zones, hosts $\geq$ 74% L–V inclusions and $\leq$ 3% contain halite crystals (**Table 2**). Similar proportions of 75% L–V inclusions and 4% with a halite-crystal were documented for quartz in a sample of Ttp between the Union Hill stock and Rattlesnake fracture zone (**Table 2**). Whereas fluid inclusions hosted by quartz in breccia that formed during emplacement of the Tqtp stock consist of 45% L–V, 45% V–L, 6% with a halite-crystal, and 4% with a sylvite crystal (**Table 2**). Two samples of quartz from fracture zones in Ttp host $\geq$ 72% V–L inclusions and 5% contain a halite crystal (**Table 2**). Finally, primary S–L–V inclusions were most abundant in quartz from a section of the Rattlesnake fracture zone that experienced potassium metasomatism, as indicated by 26% halite-bearing inclusions and 19% halite–sylvite bearing inclusions (**Table 2**).

Additional reconnaissance studies of fluid inclusions in mineralized quartz from fracture zones, intrusion breccia, and geologic contacts identified complex polyphase inclusions. Cubic opaque crystals (**Figure 5g**) and up to five salt crystals with different habits (some birefringent) were identified in primary inclusions (**Figure 5h**). Additionally, sylvite crystals were only identified in auriferous samples from fracture zones, breccia, and proximal to geologic contacts.

5.4 Metal contents and zoning

The ranges in metal contents and calculated averages for different rock and alteration types are presented in Appendix B. Samples of breccia and zones of potassium metasomatism in Ttp contain high concentrations and the greatest average values for Au–Ag–W–Sn–Cu–Mo–F. However, some samples of unaltered to weakly altered Tqtp contain high concentrations of Au–Ag–W–As, with elevated As concentrations also occurring in breccia and zones of potassium metasomatism in Ttp. Maximum values of Pb are recorded for samples of unaltered to weakly altered Tqtp and zones of potassium metasomatism in Ttp. Even though metal concentrations in propylitized and argillized Tqtp samples are low overall, samples of propylitized Tqtp record the greatest amounts of Sb and Hg.

A vertical distribution of metals in the Dakota Maid fracture zone was determined using the whole-rock geochemical data for core samples obtained from four drill holes. These holes intersected the fracture zone at different depths over a vertical interval of 150 m. Although the concentrations of Cu–W–Sn–Mo–Zn–Pb–Sb–Hg were determined for samples of core measuring 0.9–1.6 m in length, values for Au and Ag are based on assays of 0.3-m core samples. The highest concentrations of Sb–Hg–Pb–

Table 2. Percentages of different types of primary fluid inclusions in samples of hydrothermal quartz. Sample descriptions are provided in Appendix A. Abbreviations: NA = not applicable; OFZBX = outside of fracture zones or breccia; FZ = within a fracture zone; and IBX = adjacent to intrusion breccia.

Sample Number	Liquid rich	Vapor rich	Halite bearing	Sylvite bearing	Geology
1	**79%**	18%	3%	NA	OFZBX
2	**74%**	25%	1%	NA	OFZBX
3	**75%**	22%	3%	NA	OFZBX
6	45%	45%	**6%**	**4%**	IBX
8	23%	32%	**26%**	**19%**	FZ
9	**75%**	21%	4%	NA	OFZBX
12	22%	**72%**	5%	1%	FZ
13	20%	**73%**	5%	2%	FZ

Zn–As occur near surface at elevations of 1610–1575 m (**Figure 10**). In contrast, the greatest amounts of Ag–Cu–W–Mo–F and Au–Sn occur at elevations of 1510 m and 1460 m (**Figure 10**), respectively.

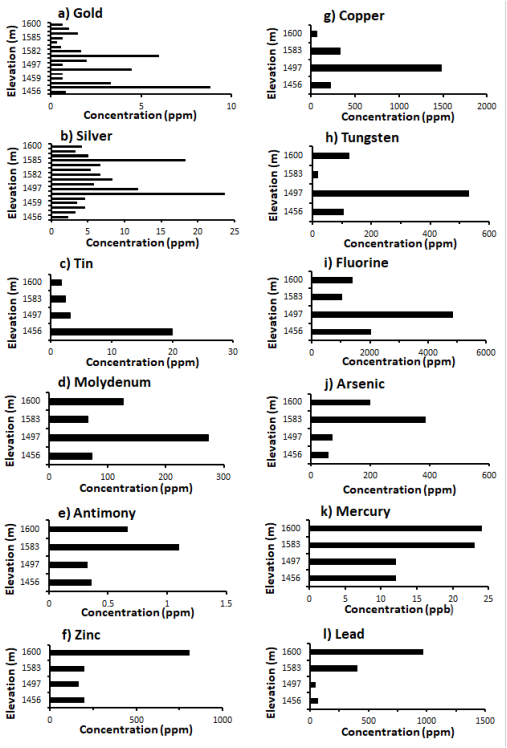

Figure 10. Plots showing the vertical distribution of metals in samples of Ttp from the Dakota Maid fracture zone. Bars indicate ranges in metal concentrations, with mercury reported as ppb compared with ppm for other metals.

The whole-rock geochemical data for additional core holes were used to document the vertical distribution of metals at a deposit scale for unaltered to weakly altered Tqtp, propylitized Tqtp, and zones of potassium metasomatism in Ttp. Mineralization in the unaltered to weakly altered Tqtp occurs in discrete zones compared with disseminated mineralization over larger intervals in propylitized Tqtp. A total of 92 core samples spanning a 460-m vertical interval were used to determine the distribution of metals in unaltered to weakly altered Tqtp. The highest values of Mo–As–Pb (–Zn–F) occur at elevations above 1410 m (**Figure 11**). Whereas the concentrations of Cu–W peak at an elevation of 1300 m and then decrease abruptly with depth. Finally, high values for Au and Ag overlap between elevations of 1350–1250 m but then high gold values extend downward to an elevation of 1160 m (**Figure 11**).

A smaller data base consisting of 24 core samples spanning a vertical interval of 424 m was used to study the distribution of metals in propylitized Tqtp. Note that the concentrations of Au–W–Mo–Pb (**Figure 12**) are significantly lower relative to unaltered to weakly altered Tqtp **(Figure 11**). Another difference is that maximum values of Ag–Cu–Zn–Hg–Pb in propylitized Tqtp occur below an elevation of 1200 m compared with the highest concentrations of Au–W–Mo–F that occur above an elevation of 1373 m (**Figure 12**).

The final database of 65 samples for zones of potassium metasomatism in Ttp span a vertical interval of 451 m (**Figure 13**). Values for Au–Ag–W–Mo–Cu are all higher compared with propylitized and unaltered to weakly altered Tqtp (**Figures 11** and **12**). The highest concentrations of Ag–As–Zn–Pb in Ttp that experienced potassium metasomatism occur near surface between elevations of 1600–1510 m (**Figure 13**). In contrast, the highest concentrations of Au–W–Mo–Cu–F occur between elevations of 1350–1190 m (**Figure 13**).

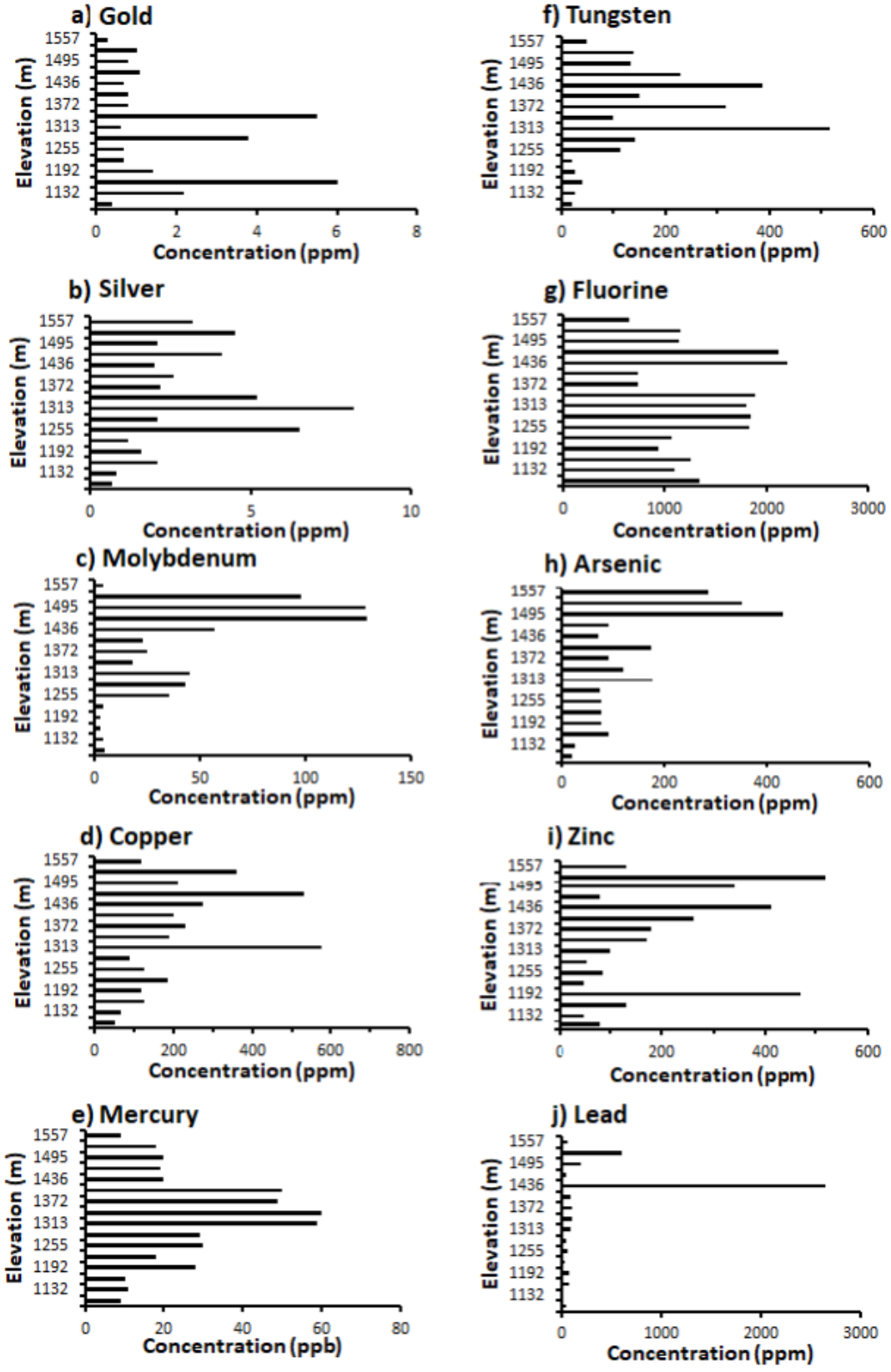

Figure 11. Plots showing the vertical distribution of metals in unaltered to weakly altered Tqtp. Bars indicate ranges in metal concentrations, with mercury reported as ppb compared with ppm for other metals.

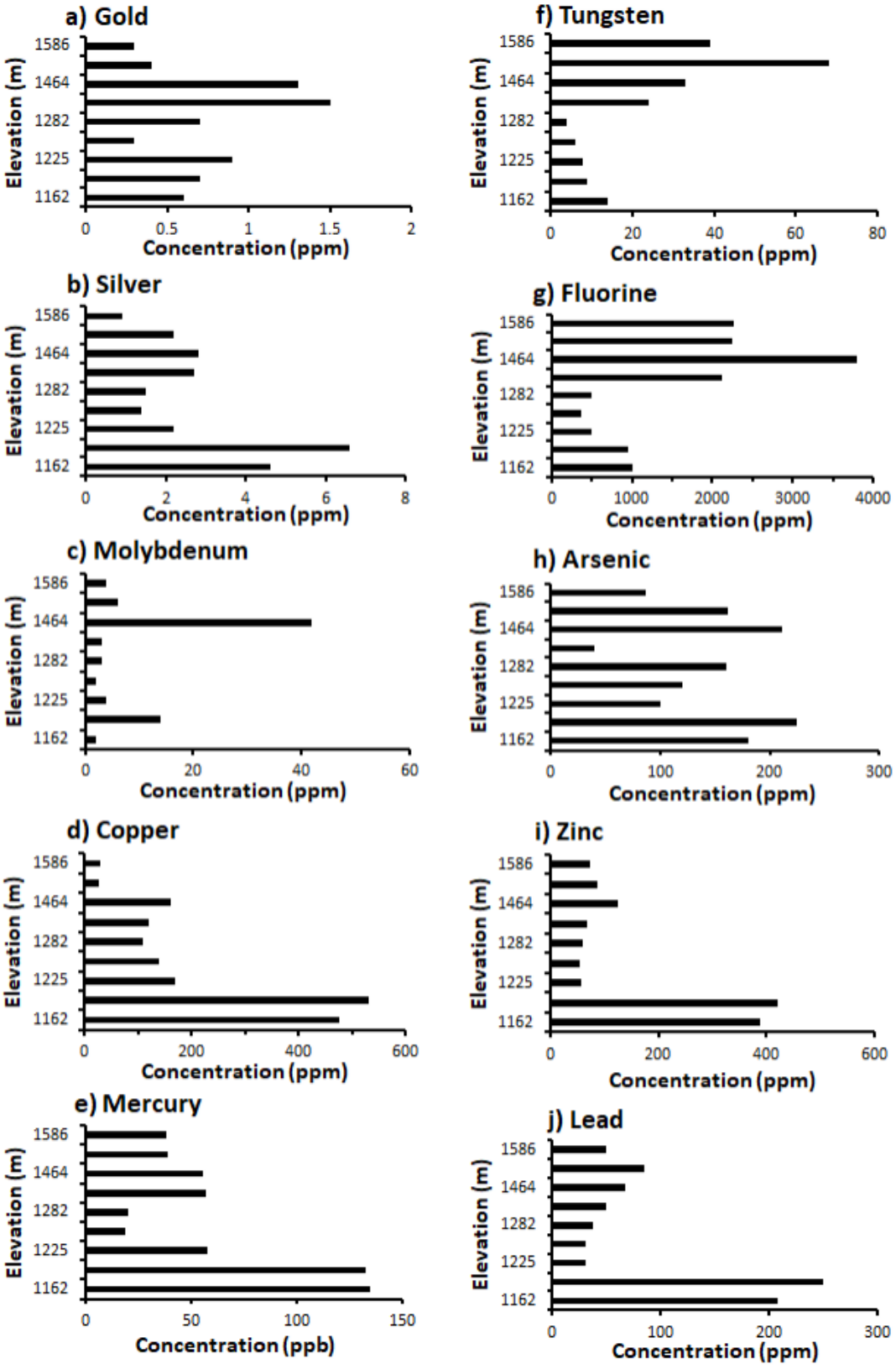

Figure 12. Plots showing the vertical distribution of metals in propylitized Tqtp. Bars indicate ranges in metal concentrations, with mercury reported as ppb compared with ppm for other metals.

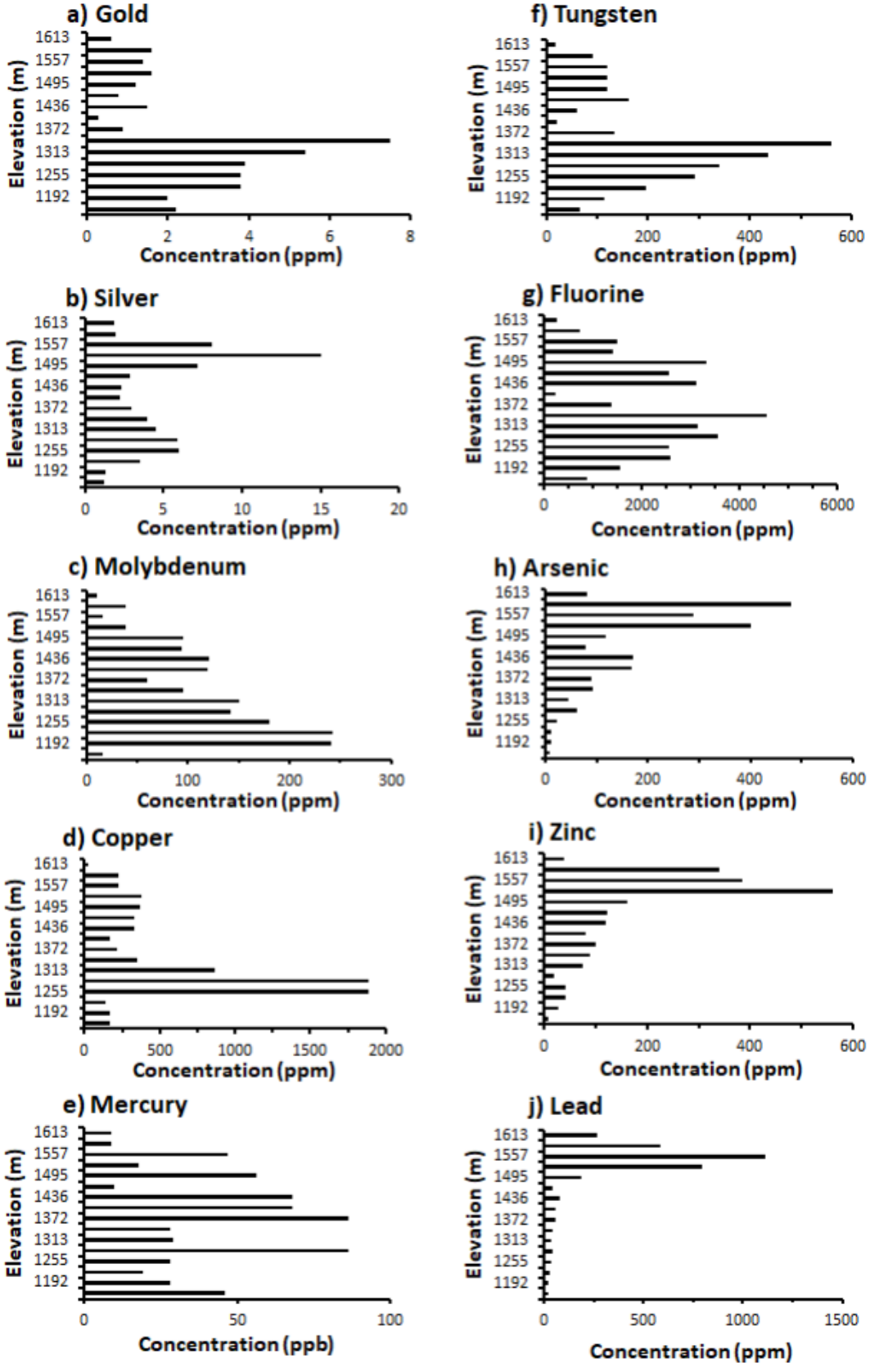

Figure 13. Plots showing the vertical distribution of metals in Ttp that experienced potassium metasomatism. Bars indicate ranges in metal concentrations, with mercury reported as ppb compared with ppm for other metals.

6. Discussion

6.1 Interpretation of Th data for fluid inclusion assemblages

The large ranges in T_h of $\leq 70°C$ for some individual fluid inclusion assemblages can potentially be explained in several ways. Fluid inclusions could be different generations; however, careful observations were made while assigning origins of primary versus secondary based on the criteria established by Roedder [30]. There is a possibility that inclusions underwent post-entrapment modification through necking, or leakage related to younger tectonic and/or hydrothermal events. Petrographic studies of doubly polished sections did identify a small number of fluid inclusions in the process of necking down, but these were excluded from analyses. Evidence against the modification of inclusions by younger tectonic and/or hydrothermal events includes the different types of primary inclusions (e.g., S–V–L, V–L, and L–V) versus secondary inclusions (e.g., V–L or V) hosted by pre-ore hydrothermal quartz veins (sample 18). Distinct assemblages of fluid inclusions hosted by hydrothermal quartz in ore samples from different geologic settings were also documented by point counts (**Table 2**). A final piece of supporting evidence is that complex fluid compositions documented by inclusions containing up to five multiple transparent crystals and an opaque crystal were limited to quartz from structural zones.

An alternative explanation for the large ranges in T_h for individual inclusion assemblages could be that steep temperature gradients existed during mineralization, or conditions underwent rapid change during formation of the intrusive complex. Temperature gradients certainly existed across the deposit and into country rocks, but the T_h range of $\leq 70°C$ for individual fluid inclusion assemblages is problematic due to a scale of < 1 mm. An important commonality between these samples is that all of the fluid inclusion assemblages contain a mixture of L–V, V–L, and S–L–V inclusions. This suggests the trapping of a heterogeneous fluid, which is supported by the overlap of $T_{h(v)}$and $T_{h(L)}$. In contrast, samples from the interior of the Tqtp stocks that contain assemblages of L–V inclusions homogenize specifically to the liquid phase and record ranges in T_h of $\leq 30°C$. Therefore, the most-representative conditions for mineralization where fluid inclusion assemblages record large ranges in T_h would be the overlapping $T_{h(v)}$and $T_{h(L)}$. This includes temperature ranges of 280o–350°C for Tqtp adjacent to breccia that formed during emplacement of the stocks and 385o–500°C for fracture zones.

Inclusions that trapped a heterogeneous fluid at shallow depths would require a minimal pressure correction to T_h. The reactivation of faults in Precambrian basement rocks, strong structural control of mineralization, open-space fillings, and miarolitic cavities (**Figure 7**) support an open system and hydrostatic pressure conditions. A maximum depth for mineralization of 1.6 km is based on the stratigraphic reconstruction by Paterson et al. [34]. By using these data and the graphs of Potter [35], pressure corrections would be $\leq$ 20oC for T_h of 285°–400°C.

6.2 Magmatic differentiation and degassing

A primary objective of the current study was to generate fluid inclusion data to test the hypothesis that oxidized magmas released a volatile-rich low-density fluid associated with gold mineralization. The two, distinct fluid inclusion assemblages hosted by primary quartz in unaltered Ttp record phase separation at 700°C that produced a residual oxidized magma based on the identification of red hematite crystals in some S–L–V inclusions. If H_2S partitioned into the low-density fluid, then the remaining high-density phase would be oxidized [16, 36]. Evidence for the partitioning of H_2S into a low-density fluid includes hydrothermal quartz in structural zones hosting inclusions with opaque sub-round and cubic (pyrite) crystals (**Figure 5g**). Pyritization during mineralization is also indicated by the abundance of veins/veinlets, coarse disseminations in argillized rocks, and the matrix to breccia.

The reactivation of structures in Precambrian rocks provided pathways for the ascent of low-density volatile-rich fluids produced during differentiation in a deep magma chamber. Evidence for this includes the multiple trains of crosscutting V–L and one-phase vapor inclusions in pre-gold hydrothermal quartz veins (**Figure**

5c); fluid inclusion assemblages in ore-stage quartz from fracture zones and breccia being dominated by V–L inclusions (**Table 2**); and miarolitic cavities in the matrix of auriferous breccia samples (**Figure 7**) that record a fluid phase [37]. Due to changes in pressure and temperature during ascent, vapor contraction would occur to form a hypersaline fluid [38]. The best example of this at the Gilt Edge mine is an area of potassium metasomatism in the Rattlesnake fracture zone, where native gold is intergrown with hydrothermal quartz hosting a large population of S–L–V fluid inclusions (**Table 2**; **Figure 9**).

The low-density volatile-rich fluid that accumulated at the apex of a deep magma chamber would have a complex composition (e.g., Na, K, F, Cl, S, H_2O, CO_2 [7]) and might be recognizable in the hydrothermal system. This is the case at the Gilt Edge mine because fluid mixing did not occur in the primary structures through which auriferous fluids ascended. Complex fluid compositions are recorded by inclusions containing up to five transparent crystals (some birefringent) $\pm$ opaque crystals in hydrothermal quartz from fracture zones and breccia (**Figure 5g,h**). Similarly, depressed eutectic temperatures of –23o to –32oC were only measured for L–V inclusions in ore samples from fracture zones and breccia. These overlap with eutectic temperatures of –24.3° to –35.4°C for fluid inclusions in a Au–Te epithermal deposit related to porphyry copper mineralization in the Fakos Peninsula, Greece and suggest the presence Ca, Fe, and/or Mg salts [39, 40]. A final point concerning the Gilt Edge deposit is that there are instances where quartz in fracture zones that underwent potassium metasomatism host inclusions with different-sized round crystals having identical optical properties that melted at the same temperature **(Figure 5i**), which could indicate saturation of the auriferous fluid with KCl.

This diverse suite of transparent and opaque crystals hosted by fluid inclusions in hydrothermal quartz from structural zones does not reflect large-scale fluid circulation and the leaching of different elements from country rocks. Geological relationships indicate that fluid flow was fracture controlled, there is little alteration beyond permeable zones, and some alteration of the igneous rocks was deuteric [21, 23]. Whereas magmatic differentiation in a deep chamber is supported by a change with time from more mafic (Thtp) to felsic (rhyolite) igneous rocks; a progression in feldspar compositions from Or_{30} (Thtp) to Or_{68} (rhyolite) [23]; and the presence of fluorite veins and matrix to breccia. The latter is relevant because fluorine decreases magma viscosity by lowering the magma solidus, which extends the period of crystallization and allows for a high degree of fractionation [41, 42].

These processes were not unique to the Gilt Edge deposit, as magma degassing is documented by geological relationships at other locations in the northern Black Hills, Wyoming, and Montana. The Lead–Deadwood dome area encompasses the Richmond Hill deposit hosted by a breccia pipe [43]; there are breccia dikes associated with Tertiary intrusions at the Homestake mine [44]; and dikes extend to sills of polymictic breccia that overlap or occur proximal to ore zones in the Golden Reward mine [45]. Exotic clasts of Precambrian rocks are common and have been identified 50 meters above the Precambrian–Cambrian unconformity, which indicates emplacement in a fluid state under high pressure. Finally, breccia pipes associated with Tertiary igneous rocks in the Lead–Deadwood, Tinton, and Bear Lodge domes all contain exotic clasts that include underlying Precambrian units [44].

A deep fluid source also supplied metals based on the vertical distribution of metals at the Gilt Edge and Homestake mines. Microthermometric data for S–L–V, L–V, and V–L primary inclusions in ore samples from fracture zones and breccia record the highest T_h and salinities for auriferous fluids (**Figures 9** and **14**). The ascent and cooling of these magmatically derived fluids in primary structures deposited metals in specific sequences. Metal zoning in the Dakota Maid fracture zone consists of near surface (1610–1575 m) Sb–Hg–Pb–Zn–As and deeper Au–Sn (**Figure 10**). The whole-rock geochemical data for zones of potassium metasomatism in Ttp at a deposit scale also record near surface (1600–1510 m) Ag–Pb–Zn–As and deep Au–W–Mo–Co (**Figure 13**). Although whole-rock geochemical data for the Homestake mine are not available, a zoning of minerals records shallow Cu–Zn–Pb–Ag and deep Au–Mo–Bi centered on a Tertiary rhyolitic dike complex [46].

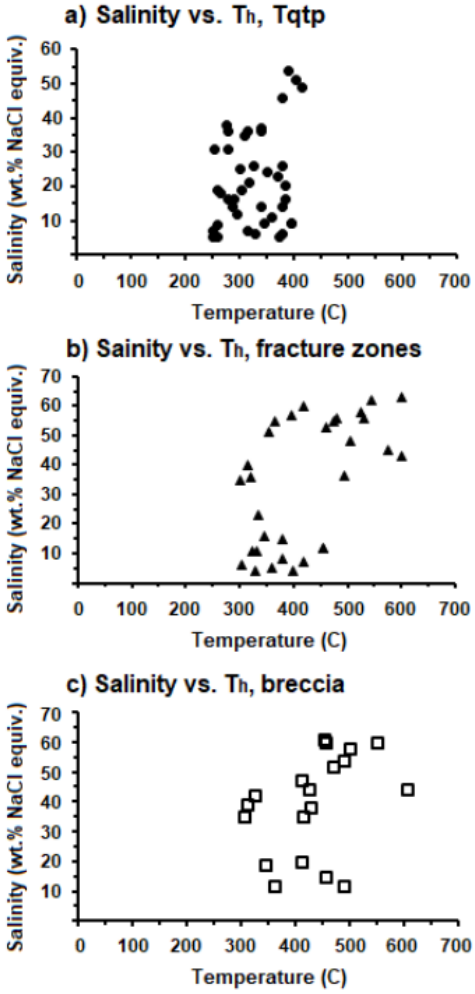

Figure 14. Salinity vs. Th diagrams for ore samples from **a**) Tqtp, **b**) fracture zones, and **c**) breccia.

6.3 Mineral paragenesis and gold complexing

The occurrence of gold in mineralogically distinct stages of the paragenesis could suggest different complexing agents. Stage 1 hydrothermal fluids caused potassium metasomatism of Ttp and deposited both native gold and silver in fracture zones. Fluid inclusion data for quartz intergrown with native Au and hydrothermal adularia record the highest T_h and salinities for all types of alteration (**Figure 9**); fluid inclusion assemblages consist of nearly half S–L–V inclusions (**Table 2**); and this hydrothermal quartz has the heaviest $\delta 18O_{H2O}$ values of 9.3–10.4‰ [20]. All of which provide evidence for a magmatic source of fluids and the high salinities support gold being transported by chloride complexes. Specifically, $AuCl(H_2O)_y$ has a maximum solubility at 460oC for an intermediate-density fluid [47] and this overlaps the T_h of fluids that produced potassium metasomatism and high-grade gold mineralization in the Rattlesnake fracture zone (**Figure 9c**). Boiling likely occurred due to tectonic decompression related to the reactivation of fracture zones sealed by quartz and sulfides. The abrupt changes in concentrations of Au–W–Mo–Cu (–F) between elevations of 1350–1190 m (**Figure 13**) could mark a boiling zone. Fluid mixing in this zone is not indicated due to the significant population of S–L–V inclusions (**Table 2**) and heavy $\delta 18O_{H2O}$ values for hydrothermal quartz.

Stage 2 mineralization is characterized by changes in oxygen fugacity. Fluctuating conditions resulted in pyrite replacing primary iron-oxide minerals and then a second generation of iron-oxide minerals replacing pyrite (**Figures 3** and **4b**). Gold deposition occurred with the period of pyrite stability between mineralogical changes involving magnetite–hematite. This stage of mineralization is the most widespread due to occurring within the Tqtp stocks, breccia, and fracture zones.

Changes in oxygen fugacity could be related to evolution of the Tqtp stocks and fluid mixing. Emplacement of the Tqtp stocks was a two-step process that involved ponding at depth, as indicated by $\leq$ 5-cm phenocrysts set in a cryptocrystalline groundmass. Goldfarb and Pitcairn [48] considered ponding to be an essential step in ore genesis that allowed for metal concentration prior to emplacement at shallow crustal levels. If the Tqtp stocks underwent degassing at depth, then the resulting oxidized melt could precipitate primary iron-oxide minerals. After emplacement of the Tqtp stocks, meteoric water entered the hydrothermal system based on $\delta 18O_{H2O}$ values of 3.2–4.7‰ for argillized Tqtp [20] and the distribution of data in a salinity vs. T_h plot that supports mixing of high- and low-salinity fluids (**Figure 14a**). The circulation of this mixed hydrothermal fluid may have redistributed metals based on different zoning patterns for Ttp that experienced potassium metasomatism versus unaltered to weakly altered Tqtp (**Figures 11** and **13**).

Following the second and final redox change in Stage 2, native gold was deposited as inclusions in ar-

senopyrite, loellingite, and chalcopyrite. At temperatures $\leq$ 275oC experimental data document that Au–S complexes dominate over Au–Cl complexes in a medium-density fluid [19]. Therefore, late mineralization in Stage 2 was likely due to the destabilization of Au–S complexes caused by cooling and fluid mixing, prior to the next injection of a volatile-rich low-density fluid into the hydrothermal system.

Stage 3 mineralization is recognized by the presence of Au–Ag tellurides in structural zones and proximal to geologic contacts. As fluid inclusion assemblages in samples from these localities record the trapping of a heterogeneous fluid (**Figure 4**; **Table 2**), gold was likely transported in the vapor phase by Te complexes based on the thermodynamic properties of aqueous Te species [49]. Concentrations for Te of several ppm can exist in a slightly reduced 300oC vapor but at temperatures $\leq$ 505o C, Te (IV) has the highest solubility of a tellurium specie [50]. Mechanisms that cause gold deposition from Te complexes include multi-stage boiling, the condensation of a magmatically derived vapor phase upon encountering hydrothermal fluids, and fluid–rock interaction [50, 51]. Although boiling occurred in the Gilt Edge hydrothermal system, the distribution of data in salinity versus T_h diagrams for ore samples from fracture and breccia zones supports mixing between highly saline and lower salinity fluids (**Figures 14b,c**). The $\delta 18O_{H2O}$ values of 6.0–7.7‰ for samples of hydrothermal quartz in structural zones are also lighter compared with data for potassium metasomatism in the Rattlesnake fracture zone [20].

6.4 Genesis of the Gilt Edge deposit

The evolution of a deep magma chamber and magma degassing were fundamental to the formation of the Gilt Edge gold deposit. Part of this is related to the saline ore fluids documented for Stages 1–3 (**Figures 6** and **14**). A comparison of high-temperature experimental data for barren vs. mineralized granites shows that exsolved fluids with low salinities were less efficient extracting metals from a melt and could not form an ore deposit [52]. Furthermore, results of high-temperature experiments record a correlation of Au and Cl contents in magmatic vapors [53]. The timing of sulfide saturation was also critical because if it occurred early in the magma's crystallization and sulfides precipitated, a vapor phase that exsolved later would not contain appreciable amounts of Au and Cu [17]. Whereas a sulfide-undersaturated magma that underwent $\geq$ 70% fractionation would concentrate Au–Cu–S–Cl into an exsolved low-density fluid [54, 55]. Gold mineralization in the Gilt Edge deposit was associated with Tqtp stocks, which represent the third and last major phase of igneous activity that formed the intrusive complex.

There were multiple episodes of magma degassing with the volatile-rich low-density fluids focused along pre-existing structures in Precambrian rocks. Evidence for magma degassing and associated gold mineralization is not only provided by fluid inclusion data (**Figure 5**, **Table 2**), but ore textures as well. The first example is that miarolitic cavities, indicative of a fluid phase, were only identified in ore-grade breccia samples cemented by fluorite or containing a siliceous–pyritic matrix (**Figure 7**). A second example involves the high temperature of auriferous fluids, which is confirmed by altered clasts and a baked margin where the siliceous–pyritic matrix of breccia contacts country rock (**Figure 7a**). In contrast, clasts are not altered in breccias cemented by late-stage fluorite (**Figure 7b**) due to lower fluid temperatures (**Figure 8**), similar to those for fluorite from the Zortman–Landusky mine in Montana [13].

The reactivation of structures and overprinting of different mineralizing events (e.g., samples 8, 10, 14, 17, 21) was another important aspect of ore genesis. These same processes operated on different scales at the Axi epithermal gold deposit [56], China and the giant Grasberg deposit [57], Indonesia. Within the Gilt Edge deposit, areas of high permeability such as breccia and fracture zones in Ttp that experienced potassium metasomatism contain the greatest concentrations and average grades of Au–Ag–Cu–Mo–W (**Appendix B**). Whereas the collapse of the hydrothermal system is likely recorded by low metal concentrations in propylitized Tqtp, with the greatest amounts of Hg–Pb–Zn–Ag–Cu at depth (elevation < 1200 m; **Figure 12**). The movement of these metals likely tracked retreating isotherms in the hydrothermal system's final stage. Lower fluid temperatures and salinities near the end of the stage 3 mineralization are

indicated by the microthermometric data for propylitic alteration (**Figure 9**); followed by meteoric water forming stage 4 fluorite (**Figure 8**).

A maximum depth for mineralization is 1.6 km based on the stratigraphic reconstruction of Paterson et al.[34]. However, it is likely that erosional unroofing occurred during formation of the intrusive complex. A shallow depth of emplacement for igneous intrusions is supported by the Ttp and Tqtp stocks having chilled margins[23]. Rapid cooling, or quenching, is also indicated by the cryptocrystalline ground mass of Tqtp stocks and microcrystalline to chert-like siliceous matrix in samples of high-grade breccia (**Figure 7a**).

7. Conclusions

Gold mineralization in the Gilt Edge deposit was closely associated with magma degassing during the formation of an alkaline intrusive complex. Two distinct populations of primary fluid inclusions hosted by quartz disseminated in the groundmass of unaltered trachyte porphyry record phase separation at 700°C and the presence of a cogenetic hypersaline ($\leq$ 78 wt.% NaCl equiv.) oxidized fluid, indicated by red hematite crystals in some inclusions. Magma degassing during mineralization is supported by V–L inclusions being the dominant population for hydrothermal quartz from fracture zones and breccia. In addition, pre-ore quartz veins contain multiple trains of crosscutting vapor-rich inclusions. The volatile-rich nature of auriferous fluids is recorded by inclusions that contain up to five transparent crystals. Eutectic temperatures of –23°C to –32°C for L–V inclusions suggest the presence of Ca, Fe, and/or Mg salts. In contrast, primary fluid inclusions hosted by hydrothermal quartz in argillized and propylitized zones of quartz trachyte porphyry are dominantly L–V with rare halite or sylvite crystals and no polyphase inclusions were identified. The collapse of the hydrothermal system is recorded by late-stage fluorite that hosts L–V inclusions with T_h and salinities as low as 85°C and 0 wt.% NaCl equiv., respectively. Retreating isotherms are likely recorded by the highest concentrations of Hg–Pb–Ag–Zn at elevations < 1200 m in propylitized quartz trachyte porphyry, compared with the highest concentrations of Au–W–Mo–Cu–F for zones of potassium metasomatism in trachyte porphyry at elevations of 1350–1190 m.

Conflict of Interest

The author has no competing interests to declare.

Data Availability Statement

Confidentiality agreements with Brohm Mining Corporation preclude the release of data beyond what is presented in this paper.

Funding

This project was funded through the Department of the Interior's Minerals Institutes program administered by the Bureau of Mines [grant number G1174161], with additional support in the form of whole-rock geochemical analyses provided by Brohm Mining Corporation.

Acknowledgments

The author needs to recognize and thank several people that made important contributions to the project. Two anonymous reviewers provided thoughtful insights that improved the clarity of the manuscript. J.B. provided access to the whole-rock geochemical data and coordinated access to the core shed and pit for sampling. Discussion of the fluid inclusion microthermometric data and mineral paragenesis with C.P. also proved helpful in developing a genetic model for the Gilt Edge deposit. Finally, B.B. kindly performed Raman microprobe analyses of select fluid inclusions.

Appendix A

Descriptions of samples used for documenting mineral paragenetic relationships and *fluid inclusion microthermometry. Sample numbers correspond to those on the geologic map of the Gilt Edge deposit (**Figure 2**). Low-grade samples contain < 1 ppm gold; mid-grade samples contain 1–2 ppm gold; and high-grade samples contain $\leq$ 9 ppm gold. Abbreviations: D42/60m = the sample is from core hole 42 at a depth of 60 meters.

Sample 1 (D42/60m). *Fluid inclusion microthermometry. Union Hill Tqtp not in a structural zone, low-grade. Minor clay in vugs with mineralization consisting of pyrite and chalcopyrite disseminated in the ground mass.

Sample 2 (D42/170m). *Fluid inclusion microthermometry. Union Hill Tqtp in a zone of propylitic alteration, mid-grade. Native gold was identified in the groundmass of this sample with pyrite, magnetite, ilmenite, and hematite. The Fe-oxide minerals replace pyrite, whereas sphalerite occurs as veinlets.

Sample 3 (D42/237m). *Fluid inclusion microthermometry. Union Hill Tqtp not in a structural zone, low-grade. Mineralization consists of disseminated pyrite, chalcopyrite, magnetite, ilmenite, and hematite in the ground mass. The Fe-oxide minerals replace pyrite, and a second generation of pyrite occurs as veinlets.

Sample 4 (D22/327m). *Fluid inclusion microthermometry. Union Hill Tqtp in an argillically altered area 30 m from the contact with Ttp, mid-grade. Mineralization also occurs as disseminations of pyrite (containing inclusions of pyrrhotite), chalcopyrite after pyrite in the groundmass, and veinlets of sphalerite.

Sample 5 (D37/141m). *Fluid inclusion microthermometry. Union Hill Tqtp not in a structural zone, low grade. Mineralization consists of disseminated pyrite (containing inclusions of Pb), pyrrhotite, and magnetite in the groundmass. A second generation of pyrite occurs as veinlets.

Sample 6 (D40/178m). *Fluid inclusion microthermometry. Union Hill Tqtp that contains xenoliths and is adjacent to a zone of intrusion breccia, low-grade. Mineralization consists of disseminated pyrite (containing inclusions of pyrrhotite and magnetite), chalcopyrite, and magnetite in the groundmass. Chalcocite rims chalcopyrite in the groundmass but does not occur as veinlets.

Sample 7 (D25/191m). *Fluid inclusion microthermometry. Unaltered Rattlesnake Ttp 10 m east of the Rattlesnake fracture zone, low grade. Mineralization consists of disseminated pyrite, pyrrhotite, chalcopyrite, magnetite, ilmenite, and hematite in the ground mass. There are rare 5-mm pyrite veinlets and one contains intergrown purple fluorite.

Sample 8 (D25/205m). *Fluid inclusion microthermometry. Area of potassium metasomatism in the Rattlesnake fracture zone, high grade. There is nearly complete replacement of Ttp by secondary adularia and fine-grained hydrothermal quartz. Native gold is intergrown with quartz, but native silver occurs in a vug. Additional mineralization consists of disseminated pyrite rimmed by marcasite or hematite and magnetite with inclusions of pyrrhotite in pyrite.

Sample 9 (D25/249m). Rattlesnake Ttp located between the Rattlesnake fracture zone and the Union Hill Tqtp stock, low grade. Mineralization consists of disseminated pyrite and chalcopyrite in the groundmass.

Sample 10 (D6/259m). *Fluid inclusion microthermometry. Intrusion breccia partly surrounding the Langley stock, mid-grade. Matrix mineralization consists of intergrown quartz, pyrite, ilmenite, and chalcopyrite. The pyrite occurs as disseminations containing inclusions of petzite and veinlets. Although magnetite replaces pyrite, hematite laths are replaced by pyrite. Chalcopyrite is also rimmed by covellite and chalcocite, but neither occur as veinlets. The breccia matrix and clasts are cut by veinlets of purple fluorite that contain disseminated pyrite and chalcopyrite.

Sample 11 (D6/260). *Fluid inclusion microthermometry. Langley Tqtp adjacent to the intrusion brecciation, low grade. Mineralization consists of disseminated chalcopyrite and pyrite that is replaced by hematite in the groundmass. Chalcopyrite around pyrite crystals is rimmed by covellite and chalcocite, neither of which occur as veinlets.

Sample 12 (R386/246m). Tectonic breccia with clasts of Ttp and Precambrian schist surrounded by a pyrite-rich matrix containing chalcopyrite, mid-grade.

Sample 13 (D31/68m). Bleached Ttp cut by quartz veins in the Dakota Maid fracture zone, high-grade. Mineralization consists of disseminated pyrite, chalcopyrite, calaverite, and petzite in both the altered rock and quartz veins.

Sample 14 (D8762/170m). Pyrite vein in Ttp, Dakota Maid fracture zone, high grade. The pyrite contains inclusions of native gold (some rimmed by petzite) and chalcopyrite; however, pyrite does replace magnetite. A vug in the pyrite contains intergrown calaverite, hessite, and petzite.

Sample 15 (D8762/184m). Bleached zone in Ttp, Dakota Maid fracture zone, mid-grade. Mineralization consists of pyrite and chalcopyrite in the groundmass. Native gold occurs along fractures in pyrite crystals.

Sample 16 (D8/71m). Intrusion breccia adjacent to the Union Hill Tqtp stock, mid-grade. Clasts of Ttp contain disseminated molybdenite, pyrite, and chalcopyrite. Mineralization in the pyritic matrix includes chalcopyrite, bornite, covellite, and chalcocite.

Sample 17 (D28/71). Intrusion breccia adjacent to the Union Hill Tqtp stock, high-grade. Mineralization in the pyritic cement includes native gold, acanthite, chalcopyrite, and pyrrhotite.

Sample 18 (pit sample). *Fluid inclusion microthermometry. Quartz-veined Ttp xenolith near the margin of the Union Hill Tqtp stock. Mineralization occurs as disseminations of pyrite and chalcopyrite in both the trachyte and quartz vein. However, molybdenite was only identified in the quartz vein.

Sample 19 (R551/138). Quartz-veined Ttp in the Hoodoo fracture zone, mid-grade mineralization occurs as disseminations of pyrite and chalcopyrite, with chalcocite after chalcopyrite.

Sample 20 (D37/65). Bleached and quartz-veined Ttp in the Dakota Maid fracture zone, mid-grade. Mineralization occurs as disseminations of pyrite, chalcopyrite, and tellurides.

Sample 21 (R386/246). Highly fractured and quartz veined Ttp in the #11 fracture zone, mid-grade. Pyrite occurs as disseminations and veinlets, whereas chalcopyrite only occurs as disseminations.

Sample 22 (R548/362). Highly fractured Ttp with quartz and fluorite veinlets in the Union Hill fracture zone, high-grade. Mineralization occurs as disseminations of pyrite and chalcopyrite.

Appendix B

Metal contents in weakly altered to unaltered Tqtp, propylitized Tqtp, argillized Tqtp, potassium metasomatism (K-meta) of Ttp, and breccia. Values are report below as the maximum, minimum, and average. Units are ppb for Hg and ppm for all other metals. Unaltered Tqtp (92) indicates there are 92 samples of Unaltered Tqtp.

Unaltered Tqtp (92): Au 0.1, **5.6**, 0.3; Ag 0.1, 7.7, 1.7; As 1, **433**, 45; W 35, **500**, 56; Sn 1, **5.6**, 1.2; F 230, 2300, 890

Propylitized Tqtp (24): Au 0.1, 1.3, 0.2; Ag 0.4, 1.3, 0.9; As 28, 233, **90**; W 1, 46, 20; Sn 0.8, 1.3, 1.1; F 150, 2280, 1010

Argillized Tqtp (17): Au 0.1, 0.5, 0.2; Ag 0.4, 2.6, 1.3; As 18, 255, 47; W 1, 43, 18; Sn 0.8, 1.4, 0.9; F 450, 950, 600

K-meta Ttp (65): Au 0.1, **7.3**, **1.3**; Ag 0.5. **15**, **2.6**; As 19, **498**, **71**; W 25, **612**, **122**; Sn 1.1, **5.4** 1.3; F 250, **4450**, **1575**

Breccia (40): Au 0.4, **12.1**, **2.3**; Ag 0.5, **20.2**, **4.3**; As 1, **365**, **95**; W 17, **806**, **105**; Sn 0.8, **12**, **2**; F 980, **9250**, **2550**

Unaltered Tqtp (92): Mo 1, 105,12; Cu 3, 735, 90; Zn 32, 590, 105; Pb 50, **3530**, 90; Sb 0.1, 1.2, 0.4; Hg 8, 60, 17

Propylitized Tqtp (24): Mo 1, 40, 14; Cu 48, 509, 136; Zn 75, 475, 134; Pb 10, 225, 36; Sb 0.4, **13.5**, **1.3**; Hg 9, **135**, **48**

Argillized Tqtp (17): Mo 1, 28, 10; Cu 1, 129, 19; Zn 25, 300, 115; Pb 2, 202, 40; Sb 0.1, 0.3, 0.2; Hg 9, 27, 14

K-meta Ttp (65): Mo 18, **234**, **68**; Cu 44, **1798**, **250**; Zn 40, **670**, 70; Pb 1, **1090**, 60; Sb 0.1, 3.8, 0.3; Hg 1, **86**, 16

Breccia (40): Mo 5, **237**, **44**; Cu 42, **2040**, **260**; Zn 80, 500, **195**; Pb 1, 125, 87; Sb 0.1, 1, 0.8; Hg 12, 36, 22

References

[1] Jensen, E.P., Barton, M.D., 2000. Gold deposits related to alkaline magmatism. SEG Reviews 13, 279–314. DOI: https://doi.org/10.5382/Rev.13.08

[2] Kelley, K.D., Spry, P.G., McLemore, V.T., et al., 2020. Alkalic-Type Epithermal Gold Deposit Model. USGS Scientific Investigations Rept. 2010–5070–R, 74p. DOI: https://doi.org/10.3133/sir20105070R

[3] Begg, G., 1996. Genesis of the Vatukoula gold deposit, Fiji [PhD thesis]. Melbourne, Australia: Monash University. pp. 1–466.

[4] Zhang, X., Spry, P.G., 1994. Petrological, mineralogical, fluid inclusion, and stable isotope studies of the Gies gold-silver telluride deposit, Judith Mountains, Montana. Econ. Geol. 89, 602–627. DOI: https://doi.org/ 10.2113/gsecongeo.89.3.602

[5] Wang, F., Liu, F.Y., Bagas, L., et al., 2022. Genesis of the Zhongshangou Au-Te deposit

linked to alkaline magmatism at the northern margin of the North China Block: Evidence from sulfides Re-Os geochronology. Ore Geology Reviews. 153, 105265, DOI: https://doi.org/10.1016/j.oregeorev.2022.105264

[6] Lang, J.R., Stanley, C.R., Thompson, J.F.H., 1995. Porphyry copper-gold deposits related to alkalic igneous rocks in the Triassic–Jurassic arc terranes of British Columbia. Arizona Geological Society Digest. 20, 291–236.

[7] Kelley, K.D., Romberger, S.B., Beaty, D.W., et al., 1998. Geochemical and geochronological constraints on the genesis of Au–Te deposits at Cripple Creek, Colorado. Econ. Geol. 93, 981–1012. DOI: https://doi.org/10.2113/gsecongeo.93.7.981

[8] Ahmad, M., Solomon, M., Walshe, J.L., 1987. Mineralogical and geochemical studies of the Emperor gold telluride deposit, Fiji. Econ. Geol. 82, 345–370. DOI: https://doi.org/10.2113/gsecongeo.82.2.345

[9] Cameron, G.H., Wall, V.J., Walshe, J.L., et al., 1995. Gold mineralization at the Porgera gold mine, Papua New Guinea, in response to fluid mixing. Australasian Institute of Mining and Metallurgy Publication Series. 9, 99–100.

[10] DeWitt, E., Foord, E.E., Zartman, R.E., et al., 1996. Chronology of Late Cretaceous igneous and hydrothermal events at the Golden Sunlight gold-silver breccia pipe, southwester Montana. U.S. Geological Survey Bulletin. 2155, 1–48.

[11] Mutschler, F.E., Griffen, M.E., Stevens, D.S., et al., 1985. Precious metal deposits related to alkaline rocks in the North American Cordillera–An interpretive review. South African J Geology. 88, 355–377.

[12] Pals, D.W., Spry, P.G., 2003. Telluride mineralogy of the low-sulfidation epithermal Emperor gold deposit, Vatukoula, Fiji. Mineralogy and Petrology. 79, 285–307. DOI: https://doi.org/10.1007/s00710-003-0013-5

[13] Wilson, M.R., Keyser, T.K., 1988. Geochemistry of porphyry-hosted Au-Ag deposits in the Little Rocky Mountains, Montana. Econ. Geol. 83, 1329–1346. DOI: https://doi.org/10.2113/gsecongeo.83.7.1329

[14] Kwak, T.A.P., 1990. Geochemical and temperature controls on ore mineralization at the Emperor gold mine, Vatuukoula, Fiji. J Geochemical Exploration. 36, 297–337. DOI: https://doi.org/10.1016/0375-6742(90)90059-J

[15] Richards, J.P., Kerrich, R., 1993. The Porgera gold mine, Papua New Guinea–Magmatic hydrothermal to epithermal evolution of an alkalic-type precious metal deposit. Econ Geol. 88, 1017–1052. DOI: https://doi.org/10.2113/gsecongeo.88.5.1017

[16] Müller, D., Franz, L., Herzig, P.M., Hunt, S., 2001. Potassic igneous rocks from the vicinity of epithermal gold mineralization, Lihir Island, Papua New Guinea. Lithos. 57, 163–186. DOI: https://doi.org/10.1016/S0024-4937(01)00035-4

[17] Richards, J.P., 1995. Alkalic-type epithermal gold deposits—A review. Magmas, fluids, and ore deposits. Canada Mineralogical Association Short Course Series. 23, 367–400.

[18] Sillitoe, R.H., 2010. Porphyry Copper Systems. Econ. Geol. 105, 3–41. DOI: https://doi.org/10.2113/gsecongeo.105.13

[19] Hurtig, N., Williams-Jones, A.E., 2015. Porphyry-epithermal Au–Ag–Mo ore formation by vapor-like fluids: New insights from geochemical modeling. Geology. 43, 587–590. DOI: https://doi:10.1130/G36685.1

[20] Groff, J., Paterson, C.J., 1990. Ore paragenesis and fluids in the Gilt Edge deposit, South Dakota. SEG Guidebook Series. 7, 67–72.

[21] MacLeod, R.J., Barron, J.N., 1990. The geology of the Gilt Edge gold deposit, Northern Black Hills, South Dakota. SEG Guidebook Series. 7, 60–66.

[22] Durkin, T.V., Holm, E.H., Burtts, D.K., 1999. SOUTH DAKOTA—1998 Mineral Summary Production, Exploration and Environmental Issues. SD DENR Minerals & Mining Program. pp. 1–5. Available from: http://www.state.sd.us/denr/DES/mining/mineprg.htm

[23] Mukherjee, N., 1968. Geology and mineral deposits of the Galena Gilt–Edge area, northern Black Hills, South Dakota. Dissertation, Colorado School of Mines. pp. 1–207.

[24] Lisenbee, A.L., 1981. Studies of the Tertiary intrusions of the northern Black Hills uplift, South Dakota and Wyoming—A historical review. GSA Rocky Mtn Section Ann Mtg, Field trip guidebook. pp. 106–125.

[25] Meier, L.F., 1990. Structure and ore trend description of the Homestake mine. SEG Guidebook Series. 7, 95–102.

[26] Bachman R.L., Caddey S.W., 1990. The Homestake mine, Lead, South Dakota: An overview. SEG Guidebook Series. 7, 89–94.

[27] Armstrong, R.L., Ward, P., 1991. Evolving Geographic Patterns of Cenozoic Magmatism in the North American Cordillera: The Temporal and Spatial Association of Magmatism and Metamorphic Core Complexes. J Geophysical Res. 96, 13,201–13,224. DOI: https://doi.org/10.1029/91JB00412

[28] Duke, G.I., 2009. Black Hills–Alberta carbonatite–kimberlite linear trend: Slab edge at depth? Tectonophysics. 464, 186–194. DOI: https://doi.org/10.1016/j.tecto.2008.09.034

[29] MacLeod, R.J., 1986. The geology of the Gilt Edge area, northern Black Hills of South Dakota. Thesis, South Dakota School of Mines and Technology. pp. 1–146.
[30] Roedder, E., 1984. Fluid inclusions. Reviews in Mineralogy. 12, pp. 1–646.
[31] Diamond, L.W., 1990. Fluid inclusions evidence for P-V-T-X evolution of hydrothermal solutions in late-alpine gold-quartz veins at Brusson, Val D'Ayas, northwest Italian Alps. American J Science. 290, 912–958.
[32] Goldstein, R.H., Reynolds, T.J., 1994. Systematics of fluid inclusions in diagenetic minerals: Society of Sedimentary Geologists (SEPM) Short Course. 31, pp. 1–199.
[33] Bodnar, R.J., 2003. Introduction to fluid inclusions: Mineralogical Association of Canada Short Course. 32, 81–99.
[34] Paterson, C.J., Uzunlar, N., Groff, J., 1989. A view through an epithermal–mesothermal precious metal system in the northern Black Hills, South Dakota: A magmatic origin for the ore-forming fluids: Econ. Geol. Monograph. 6, 564–570. DOI: https://doi.org/10.5382/Mono.06.43
[35] Potter, II, R.W., 1977. Pressure corrections for fluid-inclusion homogenization temperatures based on the volumetric properties of the system NaCl–H2O. U.S. Geol. Survey J. Res. 5, 603–607.
[36] Larocque, A.C.L., Stimac, J.A., Kieth, J.D., et al., 2000. Evidence for open-system behavior in immiscible Fe–S–O liquids in silicate magmas: Implications for contributions of metals and sulfur to ore-forming fluid. Canadian Mineralogist. 38, 1233–1249. DOI: https://doi.org/10.2113/gscanmin.38.5.1233
[37] Candela, P.A., 1997, A Review of Shallow, Ore-related Granites: Textures, Volatiles, and Ore Metals. J Petrology. 38, 1619–1633. DOI: https://doi.org/10.1093/petroj/38.12.1619
[38] Heinrich, C.A., Driesner, T., Stefansson, A., et al., 2004. Magmatic vapor contraction and the transport of gold from the porphyry environment to epithermal ore deposits. Geology. 32, 761–764. DOI: https://doi.org/10.1130/G20629.1
[39] Davis, D.W., Lowenstein, T.K., Spencer, R.J., 1990. Melting behavior of fluid inclusions in laboratory-grown halite crystals in the systems NaCl–H2O, NaCl–KCl–H2O, NaCl–MgCl2–H2O, and NaCl–CaCl2–H2O. Geochimica et Cosmochimica Acta. 54, 591-601. DOI: https://doi.org/10.1016/0016-7037(90)90355-O
[40] Fornadel, A.P., Voudouris, P.C., Spry, P.G., 2012. Mineralogical, stable isotope, and fluid inclusion studies of spatially related porphyry Cu and epithermal Au-Te mineralization, Fakos Peninsula, Limnos Island, Greece. Mineralogy Petrology. 105, 85–111. https://doi.org/10.1007/s00710-012-0196-8
[41] Audetat, A., 2015. Compositional evolution and formation conditions of magmas and fluids relative to porphyry molybdenum mineralization at Climax Colorado. J Petrol. 56, 1519–1546. DOI: https://doi.org/10.1093/petrology/egv044
[42] Fayol, N., Jebrak, M., 2017. Archean Sanukitoid gold porphyry deposits: A new understanding and genetic model from the Bachelor gold deposit, Abitibi Canada. Econ. Geol. 112, 1913–1936. DOI: https://doi.org/10.5382/econgeo.2017.4534
[43] Duex, T.A., Smith, T.J., McConnell, P.A., Osmundson, T.M., Petersen, M.A., Stanley, T.M., 1987. Geology of the Richmond Hill gold deposit. 3rd AIME Western Regional Conference on Precious Metals, Coal, and Environment, Rapid City, Sept 23–26. pp. 67–71.
[44] Lisenbee, A.L., Roggenthen, W.R., 1990. Diatremes and breccia pipes of the northern Black Hills, South Dakota–Wyoming. SEG Guidebook Series. 7, 175–181.
[45] Emmanuel, K.M., Wagner, J.J., Uzunlar, N., 1990. The relationship of gold and silver mineralization to alkalic porphyry and breccia, Golden Reward mine, Lawrence County, South Dakota. SEG Guidebook Series. 7, 140–150.
[46] Uzunlar, N., Paterson, C.J., Lisenbee, A.L., 1990. Tertiary epithermal to mesothermal porphyry-related Au-Ag mineralization in the Homestake mine, Lead, South Dakota: mineral and metal zoning. SEG Guidebook Series. 7, 119–124.
[47] Hurtig, N., Williams-Jones, A.E., 2013. An experimental study of the transport of gold through hydration of AuCl in aqueous vapour and vapour-like fluids. Geochimica et Cosmochimica Acta. 127, 305–325. DOI: https://doi:10.1016/j.gca.2013.11.029
[48] Goldfarb, R.J., Pitcairn, I., 2023. Orogenic gold: is a genetic association with magmatism realistic? Mineralium Deposita. 58, 5–35. DOI: https://doi.org/10.1007/s00126-022-01146-8
[49] McPhail, D.C., 1995. Thermodynamic properties of aqueous tellurium species between 25° and 350°. Geochimica et Cosmochimica Acta. 59, 851–866. DOI: https://doi.org/10.1016/0016-7037(94)00353-X
[50] Grundler, V., Brugger, J., Etschmann, B.E., et al., 2013. Speciation of aqueous tellurium (IV) in hydrothermal solutions and vapors, and the role of oxidized tellurium species in Te transport and gold deposition. Geochimica et Cosmochimica Acta. 120, 298–325. DOI: https://doi.org/10.1016/j.gca.2013.06.009
[51] Cooke, D.R., McPhail, D.C., 2001. Epithermal Au-Ag-Te Mineralization, Acupan, Baguio Dis-

trict, Philippines: Numerical Simulations of Mineral Deposition. Econ. Geol. 96, 109–131. DOI: https://doi.org/10.2113/gsecongeo.96.1.109

[52] Audetat, A., Pettke, T., 2003. The magmatic-hydrothermal evolution of two barren granites: a melt and fluid inclusion study of the Rito del Medio and Cañada Pinabete plutons in northern New Mexico (USA). Geochimica et Cosmochimica Acta. 67, 97–121. DOI: https://doi.org/10.1016/S0016-7037(02)01049-9

[53] Hurtig, N., Migdisov, A., Williams-Jones, A.E., 2021. Are Vapor-Like Fluids Viable Ore Fluids for Cu-Au-Mo Porphyry Ore Formation? Econ. Geol. 116, 1599–1624. DOI: https://doi:10.5382/econgeo.4835

[54] Simon, A.C., Frank, M.R., Pettke,T., et al., 2005. Gold partitioning in melt-vapor-brine systems. Geochimica et Cosmochimica Acta. 69, 3321–3335. DOI: https://doi.org/10.1016/j.gca.2005.01.028

[55] Park, J.W., Campbell, I.H., Malaviarachchi, S.P.K., et al., 2018. Chalcophile element fertility and the formation of porphyry Cu ± Au deposits. Mineralium Deposita. 54, 657–670. DOI: https://doi.org/10.1007/s00126-018-0834-0

[56] Li, N., Zhang, B., Ulrich, T., et al., 2024. Magmatic degassing controlled the metal budget of the Axi epithermal gold deposit, China. American Mineralogist. 109, 51–60. DOI: https://doi.org/10.2138/am-2022-8610

[57] Leys, C., Schwarz, A., Cloos, M., et al., 2020. Chapter 29: Grasberg Copper-Gold-(Molybdenum) Deposit: Product of Two Overlapping Porphyry Systems. SEG Special Publication 23, Geology of the World's Major Gold Deposits and Provinces, Richard H. Sillitoe, Richard J. Goldfarb, François Robert, Stuart F. Simmons. DOI: https://doi.org/10.5382/SP.23.29